Journal of Materials Chemistry A

PAPER

View Article Online
View Journal

Cite this: DOI: 10.1039/c9ta06719a

High face-on ratio isoindigo copolymers with extended nano-fibrillar networks in fullerene-based thick (>300 nm) photovoltaics achieving a high efficiency of 10.7%†

Song-Fu Liao,[ab] Chun-Fu Lu,[b] Adane Desta Fenta,[a] Chin-Ti Chen,[*a] Chi-Yang Chao*[b] and Wei-Fang Su[b]

Three D–A π-conjugated copolymers P*n*TIF (where n = 2, 4, or 6), composed of isoindigo electron acceptor units and difluorinated bithiophene (BTF) electron donor units, were synthesized and characterized. The HOMO and LUMO energy levels, solubility (and miscibility with PCBM), crystallinity (and crystalline orientation) and P*n*TIF:PCBM thin film morphology (nano-fibrillar network and phase separation) of the copolymers could be adjusted by the number (0 for **P2TIF**, 1 for **P4TIF**, 2 for **P6TIF**) of flexible 3-dodecylthiophene spacers between the isoindigo and BTF units. From the tested polymer solar cells fabricated with P*n*TIF:PCBM bulk heterojunctions, **P4TIF**:$PC_{61}BM$ solar cells exhibited a remarkably high short-circuit current density of ~22 mA cm^{-2} together with a fill factor of ~61% and an open-circuit voltage >0.80 volt, resulting in a power conversion efficiency of 10.7%, making it one of the highest among $PC_{61}BM$-based polymer solar cells.

Received 24th June 2019
Accepted 19th August 2019

DOI: 10.1039/c9ta06719a

rsc.li/materials-a

1. Introduction

Nowadays, considering different options of n-type materials in bulk heterojunction (BHJ) polymer solar cells (PSCs), the highest power conversion efficiency (PCE) of single-junction binary PSCs is exceeding 11%,[1,2] 14%,[3–7] and 10% (ref. 8 and 9) for fullerene derivatives (such as $PC_{61}BM$ and $PC_{71}BM$), non-fullerene electron acceptors (NFAs), and electron-deficient polymers, respectively. Bi-continuous interpenetrating networks with fine fibril-like nanostructures have been considered as the ideal morphology of BHJ to overcome the seemingly contradictive miscibility and phase separation of p-type and n-type materials and to achieve high efficiency of PSCs. Nevertheless, such ideal nano-morphology of BHJs is not easy to achieve. Based on the chemical structures of donor (D) and acceptor (A) segments of the copolymers, the common feature of these high-performance D–π–A copolymers is oligothiophene (OT) or benzo[1,2-*b*:4,5-*b*′]dithiophene (BDT) as the donor segment. Associated with the OT unit, 2,1,3-benzothiadiazole (BT)[1,2,10,11] or naphthobisthiadiazole (NTz)[12–15] is the optimal choice for the acceptor segment of the copolymers. Regarding the BDT donor segment, thieno[3,4-*b*]thiophene (TT),[16–20] benzo[1,2-*c*:4,5-*c*′]-dithiophene-4,8-dione (BDD),[21] and 2,2′-bithiophene-3,3′-imide (BTI)[22] are the superior choices for the acceptor units. Considering their strong electron-deficient characteristics and high degree of coplanarity, isoindigo-based copolymers have been applied for PSCs in recent years.[23–35] In our previous study, we synthesized and demonstrated two isoindigo–quaterthiophene-based copolymers, *i.e.*, P4TIH and P4TIN, for high-performance PSCs (the highest PCE is 8.36%). Although a remarkably high open-circuit voltage (V_{OC}) of ~1.06 V was achieved for P4TIN:$PC_{61}BM$ PSCs, P4TIN exhibited lower crystallinity and less nano-fibrillar structure due to its non-planar conformation and a relatively large dihedral angle (~18.6°) of 3,3′-dicyano-2,2′-bithiophene (BTCN) units.[36] For further improving the performance of isoindigo–oligothiophene copolymer PSCs, we designed and synthesized a series of fluorine-substituted copolymers, **P2TIF**, **P4TIF**, and **P6TIF** (Scheme 1), of which 3,3′-difluoro-2,2′-bithiophene (BTF) unit is the common part of oligothiophene as the donor segment of the copolymers.[37]

The results presented herein indicate that **P4TIF** having the optimal isoindigo–oligothiophene repeating unit exhibits intermediate solubility and crystallinity to form an ideal morphology of interpenetrating networks with fine fibril-like structures in the active layer of **P4TIF**:$PC_{61}BM$ BHJ. PSCs having an active layer of ~300 nm thickness and a high PCE

[a]Institute of Chemistry, Academia Sinica, No. 128, Academia Road, Sec. 2, Taipei 11529, Taiwan, Republic of China. E-mail: chintchen@gate.sinica.edu.tw

[b]Department of Materials Science and Engineering, National Taiwan University, No. 1, Roosevelt Road, Sec. 4, Taipei 10617, Taiwan, Republic of China. E-mail: cychao138@ntu.edu.tw

† Electronic supplementary information (ESI) available: Details of synthesis procedures, ^{1}H NMR, GPC, TGA, DSC, UV-vis. absorption spectra, DFT simulations, SCLC data, GIWAXS analysis and TEM images for all P*n*TIF copolymers. See DOI: 10.1039/c9ta06719a

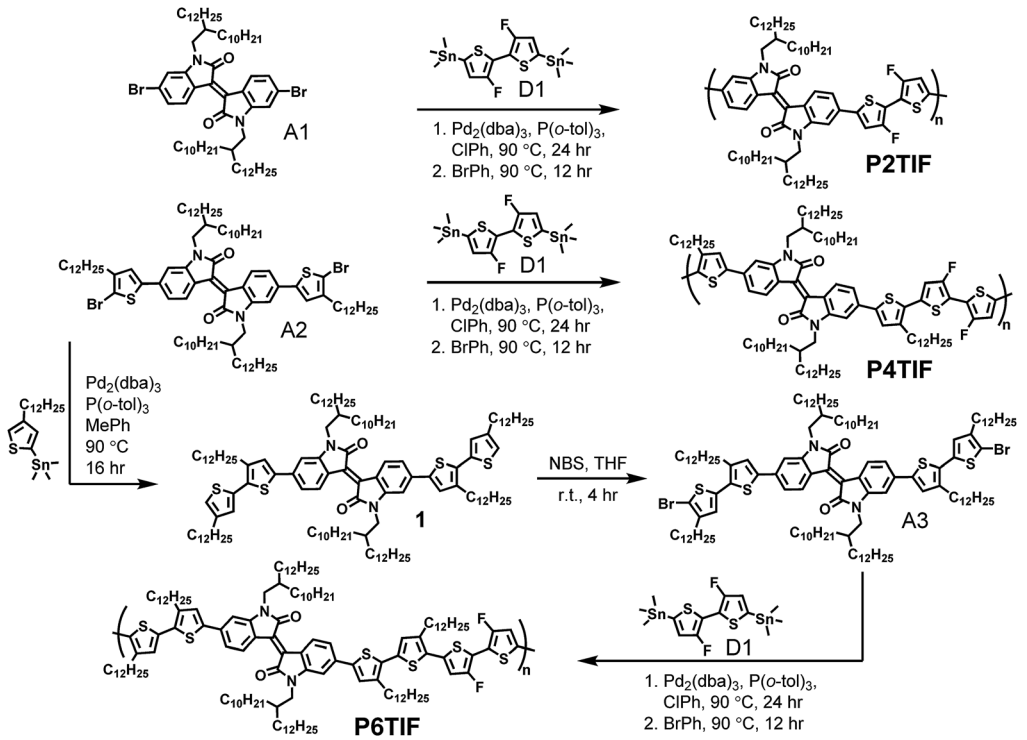

Scheme 1 Synthesis of the P*n*TIF copolymers. The donor segments of P*n*TIF are difluoro-substituted bithiophene, quaterthiophene, and sexithiophene for **P2TIF**, **P4TIF**, and **P6TIF**, respectively.

reaching 10.69% was achieved. In addition to the potentials of mass production by solution processes, our devices have an edge-on fabrication cost over other high-performance PSCs, which are usually based on much more expensive fullerene derivative, such as $PC_{71}BM$.

2. Experimental sections

2.1 Materials

The detailed synthesis procedures and identifications of the monomer (*E*)-6,6′-bis(5′-bromo-3,4′-didodecyl-[2,2′-bithiophen]-5-yl)-1,1′-bis(2-decyltetradecyl)-[3,3′-biindolinylidene]-2,2′-dione (A3) and P*n*TIF copolymers are described in ESI.† The compound (4-dodecylthiophen-2-yl)trimethylstannane,[38] the monomer (3,3′-difluoro-[2,2′-bithiophene]-5,5′-diyl)bis(trimethylsilane) (D1),[39] (*E*)-6,6′-dibromo-1,1′-bis(2-decyltetradecyl)-[3,3′-biindolinylidene]-2,2′-dione (A1),[36] and (*E*)-6,6′-bis(5-bromo-4-dodecylthiophen-2-yl)-1,1′-bis(2-decyltetradecyl)-[3,3′-biindolinylidene]-2,2′-dione (A2)[36] were synthesized according to the methods reported in the literature. The details of synthesis and chemical structural characterizations (^{1}H NMR, ^{13}C NMR, HRMS, elemental analysis, GPC) of compound 1, A3, **P2TIF**, **P4TIF**, and **P6TIF** can be found in Section S1.1 of ESI.†

2.2 Fabrication and testing of photovoltaic solar cells (PSCs)

See S2.1 and S2.2 of ESI† for details.

2.3 Fabrication of hole-only devices for space-charge-limited current (SCLC) measurement

See S5.1 of ESI† for details.

2.4 Fabrication of thin-film transistor (TFT) devices

See S5.2 of ESI† for details.

2.5 Other physical property measurements and device characterizations

The details of sample preparation and measurements for differential scanning calorimetry (DSC), thermogravimetric analysis (TGA), UV-visible absorption spectroscopy, electrochemical cyclic voltammetry (CV), density functional theory (DFT) calculations, grazing-incidence wide-angle X-ray scattering (GIWAXS), transmission electron microscopy (TEM), and atomic force microscopy (AFM) are elaborated in Sections S1.2, S3 and S4 of ESI.†

3. Results and discussion

3.1 Synthesis and characterizations of P*n*TIF polymers

The synthesis route of P*n*TIF, *i.e.*, **P2TIF**, **P4TIF**, and **P6TIF**, is illustrated in Scheme 1. Detailed synthesis procedures and structural characterizations of the reaction products can be found in ESI.† All three P*n*TIF copolymers were readily synthesized *via* a Stille cross-coupling reaction of isoindigo units (A1, A2, or A3) and a difluoro-substituted bithiophene unit (D1). **P2TIF** is composed of the monomer A1 (and D1), 3-

dodecylthiophene and bis-(3-dodecylthiophene) attached to both flanks of an isoindigo species (*i.e.*, A1) to generate A2 and A3, as the donor segment of **P4TIF** and **P6TIF**, respectively. Compared with those of **P4TIF** and **P6TIF**, the solubility of **P2TIF** is substantially lower. We have observed that **P2TIF** is prone to precipitation during the process of polymerization. In order to avoid the precipitation, which is adverse to the reaction yield, the synthesis reaction of **P2TIF** requires more solvent (almost double), *i.e.*, reaction in a more diluted solution. However, it might cause a different degree of polymerization. The **P2TIF** synthesized in this study has a much higher molecular weight than that reported in the literature.[31] Therefore, **P2TIF** synthesized in this study has significantly lower solubility than that reported in the literature.[31] The low solubility is a major adverse factor of P*n*TIF in device fabrication.

Both **P4TIF** and **P6TIF** have a similar number-average molecular weight (M_n) of 109.6 kDa and 113.2 kDa, respectively, and a similar PDI of 1.60 and 1.56 as well, respectively (Table 1). As expected, **P2TIF** has a higher M_n of 156.1 kDa and a lower PDI of 1.35 compared with those of **P4TIF** and **P6TIF**.

With additional two and four *n*-dodecyl alkyl side chains on the flanked thiophene spacers, **P4TIF** and **P6TIF** can be readily dissolved in halogenated solvents, such as chloroform (CF), chlorobenzene (CB) and 1,2-dichlorobenzene (DCB) at room temperature. However, lacking such *n*-dodecyl alkyl side chains, the solubility of **P2TIF** is much lower. The apparent solubility of P*n*TIF follows the order **P6TIF** > **P4TIF** ≫ **P2TIF**. The ^{1}H NMR spectra of **P6TIF** show the most distinguishable peaks around the aromatic shift region compared with those of **P4TIF** and **P2TIF**, indirectly verifying the suggested order of solubility (Fig. S4–S6†). Differential scanning calorimetry (DSC) determined the melting temperature (T_m) of **P2TIF** to be 388.2 °C, which is significantly higher than 295.1 °C and 251.7 °C of **P4TIF** and **P6TIF**, respectively (Fig. S7b†). In addition to the lowest solubility, the highest T_m of **P2TIF** is consistent with its strong tendency of aggregation in PSC fabrication.

3.2 Absorption spectroscopic properties

The absorption spectroscopic property of P*n*TIF copolymers in solution (CF) and thin film states was characterized using an UV-visible absorption spectrometer. The copolymer thin films were prepared by spin-coating a CF and DCB (1/1, v/v) mixed solution, which is consistent with that used in PSC fabrication. The detailed absorption data, including the wavelength of absorption maximum (λ_{max}) in solution and thin film as well as the optical bandgap (E_g^{opt}) values are listed in Table 1. As shown in Fig. 1, either in solution or thin film state, all P*n*TIF copolymers have two major absorption bands around 350–550 nm and 550–800 nm.

Comparing absorption spectra in solutions and thin films, it was observed that those of high-energy absorption bands are mostly the same, while the profile of low-energy absorption bands varied a lot due to the varied extent of intramolecular charge transfer (ICT) characteristics involved in different P*n*TIF copolymers. In the solution spectra, **P2TIF** exhibited the most distinct vibronic absorption components, *i.e.*, 0–0, 0–1, and 0–2 at 706, 647, and ~600 nm, respectively (Fig. 1a), which remain

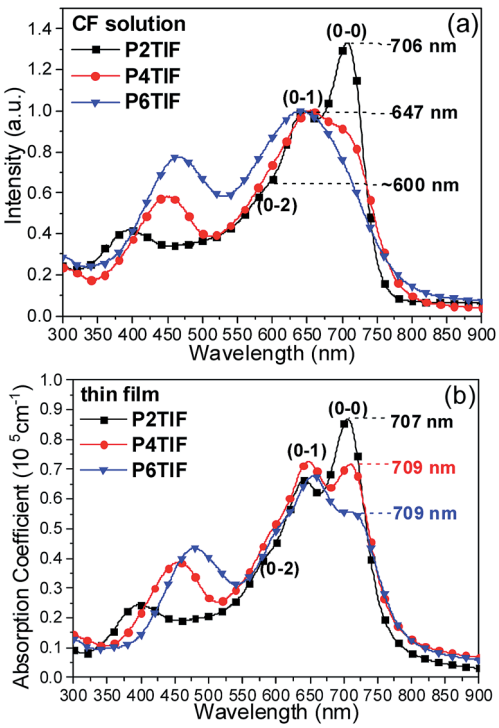

Fig. 1 UV-visible absorption spectra of P*n*TIF: (a) CF solution at room temperature. (b) Thin-film spin-coated from CF : DCB (1 : 1 volume ratio) solution.

Table 1 Characterization of P*n*TIF copolymers

P*n*TIF	M_n [kDa]	PDI	$\lambda_{high,f}/(\lambda_{high,s})^a$ [nm]	$\lambda_{0-2,f}/(\lambda_{0-2,s})^a$ [nm]	$\lambda_{0-1,f}/(\lambda_{0-1,s})^a$ [nm]	$\lambda_{0-0,f}/(\lambda_{0-0,s})^a$ [nm]	$E_g^{opt b}$ [eV]	HOMO^{CV}/LUMO^{CVc} [eV]	E_g^{CVc} [eV]	HOMO^{DFT}/LUMO^{DFTd} [eV]
P2TIF	156.1	1.35	397/(397)	~600/(~600)	642/(647)	707/(706)	1.64	−5.69/−3.82	1.87	−5.27/−2.81
P4TIF	109.6	1.60	456/(451)	~605/(unclear)	647/(655)	709/(703)	1.61	−5.41/−3.82	1.59	−4.97/−2.77
P6TIF	113.2	1.56	478/(466)	~610/(unclear)	657/(644)	709/(none)	1.58	−5.26/−3.83	1.43	−4.76/−2.76

[a] Data were obtained from UV-visible absorption spectra. $\lambda_{high,f}/(\lambda_{high,s})$: the peak max. around high-energy regions; $\lambda_{0-2,f}/(\lambda_{0-2,s})$, $\lambda_{0-1,f}/(\lambda_{0-1,s})$, and $\lambda_{0-0,f}/(\lambda_{0-0,s})$: the vibronic absorption components 0–2, 0–1, and 0–0 from each peak max., respectively (subscript "f" or "s" represents the measurements from film or solution states, respectively). [b] E_g^{opt}: the optical energy gap calculated from the onset of the lowest energetic edge of UV-visible absorption spectra in thin film state (Fig. 1b). [c] E_g^{CV}: the energy gap calculated from cyclic voltammograms (Fig. S9). [d] DFT theoretical calculation based on simplified isoindigo–oligothiophene models.

mostly unchanged in the thin film spectra, indicative of locally excited (LE) π–π* transition. On the other hand, the solution spectra of **P4TIF** and **P6TIF** have much less vibronic feature, but they are intensified in thin-film spectra. The different absorption spectra of **P4TIF** and **P6TIF** can be attributed to their more ICT characteristics and non-planar conformation, of which the stacking of polymer-chain enforces a more planar conformation in the thin film and enhances the vibronic absorption feature. Moreover, the solution absorption spectra of **P2TIF** are also consistent with the fact that **P2TIF** is the copolymer having the least non-planar conformation among P*n*TIF series, showing the least temperature dependence (Fig. S8†). The structural difference in P*n*TIF is the π-conjugation spacer, 3-dodecylthiophene, which is flexible and steric space demanding. Without any 3-dodecylthiophene in the copolymer backbone, **P2TIF** exhibits the most planar and rigid conformation and hence the lowest solubility. The significantly less ICT characteristics found for **P2TIF** than **P4TIF** or **P6TIF** may be due to the same reason, the lack of structural flexibility and steric space demanding 3-dodecylthiophene.

In addition, in the low-energy region, the thin-film absorption coefficients, of which 0–0 vibronic absorption are as high as 6.8–8.7 $\times$ 10^4 cm^{-1}, indicating an efficient absorption of solar light. These spectroscopic observations indicate that each P*n*TIF copolymers has a difference of partial ordering (or semi-crystallinity) and oriented alignment in thin film state (see Section 3.6 for details). Moreover, by introducing varied number of 3-dodecylthiophene (as the π-conjugation spacer) between isoindigo and fluorinated bithiophene (BTF) units, the E_g^{opt} and the highest occupied molecular orbital (HOMO) energy level of P*n*TIF are controllable, and the trend of V_{OC} of P*n*TIF PSCs is predictable.

3.3 Electrochemical properties and density functional theory (DFT) simulation

To more understand the influence of increasing 3-dodecylthiophene spacers between isoindigo and fluorinated bithiophene (BTF) on P*n*TIF optoelectronic properties, cyclic voltammetry (CV, Fig. S9†) and DFT simulation were performed.

As evident by the oxidation potential from CV measurements, the addition of thiophene spacer enhanced the donor strength of difluoro-substituted oligothiophene. Accordingly, the $HOMO^{CV}$ energy levels of P*n*TIF polymers were estimated to be sequentially rising as −5.69, −5.41, and −5.26 eV for **P2TIF**, **P4TIF**, and **P6TIF**, respectively (Table 1). Therefore, a relatively high and low V_{OC} can be expected for the **P2TIF** and **P6TIF** PSCs, respectively. Moreover, CV measurement reveals that all P*n*TIF show very similar reduction potentials (Fig. S9a†). Therefore, the estimated lowest unoccupied molecular orbital ($LUMO^{CV}$) energy levels of P*n*TIF are almost the same as −3.82 ± 0.01 eV (Table 1). Such results are consistent with a fact that the most electron-deficient moiety of P*n*TIF is an isoindigo unit, which is the common electron acceptor segment used in all copolymers. The $HOMO^{CV}$ energy level, which is related to the oligothiophenes, the donor segment of P*n*TIF, is the decisive factor for E_g^{CV} (the energy gap estimated by CV). E_g^{CV} was determined to be 1.87, 1.59, and 1.43 eV for **P2TIF**, **P4TIF**, and **P6TIF**, respectively. Although these values are not the same as the optical energy gaps (E_g^{opt}) estimated from the onset absorption wavelength, the trend of both E_g^{CV} and E_g^{opt} is the same, *i.e.*, **P2TIF** > **P4TIF** > **P6TIF**. The CV results shown here also provide an indirect evidence for ICT characteristics involved in the absorption band around 550–800 nm.

The HOMO and LUMO energy levels from the DFT calculations ($HOMO^{DFT}$ and $LUMO^{DFT}$) are summarized in Table 1. Although the values are different, the trend of $HOMO^{DFT}$ is exactly the same as that of $HOMO^{CV}$, *i.e.*, the sequence (from top to bottom) of the HOMO energy level is **P6TIF**, **P4TIF**, and **P2TIF**, with 0.2–0.3 eV separation in between. Similarly to those of $LUMO^{CV}$, $LUMO^{DFT}$ varied little by 0.01–0.04 eV for P*n*TIF. Analyzing HOMOs and LUMOs from the electron density contour plots (Fig. S10†), the LUMO of three copolymers encompasses a rather similar segment including isoindigo π-conjugation unit and the first thiophene ring attached to it. The oligothiophene π-conjugation unit is the main area covered by HOMO of all three copolymers. However, **P6TIF** has a HOMO extended to the adjacent benzene ring of isoindigo. The HOMO of **P4TIF** extends further to include the central CC double bond of isoindigo. Very differently, the HOMO of **P2TIF** surrounds the whole π-conjugation from oligothiophene to isoindigo. We believe that the unique HOMO constitution of **P2TIF** causes its absorption spectra different (in terms of less ICT characteristics) from those of **P4TIF** and **P6TIF**.

DFT calculations also provide a useful information about the coplanarity of the π-conjugation system, which constitutes the copolymer backbone structure of P*n*TIF. The coplanarity of the π-conjugation system is one of the two factors influential to the solubility and the aggregation (or stacking) of copolymers in solution and in thin film state, respectively. As shown in the results (Fig. S10†), the dihedral angle of fluorinated bithiophene unit (θ_{FF}) is only 0.3–0.4 degree in all three P*n*TIF, enabling a very flat or coplanar conformation. However, the dihedral angles between other adjacent aromatic rings, 3-ethylthiophene and 3-fluorothiophene (θ_{TF}), 3-ethylthiophene and 3-ethylthiophene (θ_{TT}), 3-ethylthiophene and benzene ring of isoindigo (θ_{IT}), and 3-fluorothiophene and benzene ring of isoindigo (θ_{IF}) are much larger of 12.2–15.4 degree (θ_{TF}, θ_{TT}) and 20.2–22.6 degree (θ_{IT}, θ_{IF}). When the number of alkylated thiophene spacers increased, the π-conjugation copolymer backbone becomes more twisted, which increases the non-coplanarity of the copolymer and reduces the tendency of aggregation or crystallite formation of copolymers in solution and thin film state, respectively. Thus, **P2TIF**, without any 3-dodecylthiophene spacer, has the most rigid and coplanar conformation of the copolymer backbone, which is prone to the formation of aggregate or crystallite in the thin film state. In contrast, **P6TIF** will be the most difficult one forming an aggregate or a crystallite in thin film state, and the best solubility can be expected among P*n*TIF.

3.4 Photovoltaic characteristics

The BHJ solar cells were fabricated as inverted PSCs (device area: 0.04 cm^2) with a configuration of ITO/ZnO/PEIE/

copolymer:PCBM/MoO_3/Ag. Ethoxylated polyethylenimine (PEIE) was applied to modify the surface and work function of ZnO layers.[40] Table 2 summarizes the photovoltaic characteristics of various combinations of P*n*TIF copolymers and PCBMs with or without the solvent additive diphenyl ether (DPE) (2 vol% of the mixed solvent CF/DCB).

In our device fabrication, DPE was only adopted in the fabrication of the best PSCs of P*n*TIF:$PC_{61}BM$ or $PC_{71}BM$ for final optimization. The best PSCs are **P2TIF**:$PC_{61}BM$, **P4TIF**:$PC_{61}BM$, and **P6TIF**:$PC_{71}BM$ for each P*n*TIF, respectively. As shown in the results, the effect of solvent additive DPE is copolymer dependent. For **P2TIF**:$PC_{61}BM$ PSCs, DPE improves the average power conversion efficiency (PCE) from 3.27% to 4.52%. These values are much lower than 8.8% reported in the literature.[31] However, the M_n of literature **P2TIF** (PiI2fT) is 91.6 kDa, which is significantly lower than 156.1 kDa of **P2TIF** that we synthesized in this study. The higher the molecular weight, the lower the solubility of the copolymer, hindering the preparation of PCBM-blended thin films with good nanomorphology. For **P4TIF**:$PC_{61}BM$ PSCs, DPE decreases the average PCE from 10.16% to 9.42%. For **P6TIF**:$PC_{71}BM$ PSCs, DPE decreases the average PCE from 8.35% to 7.22%. From the data listed in Table 2, the decrease or increase in PCE caused by DPE is primarily determined by the changes in the fill factor (FF) and secondarily by the short-circuit current density (J_{SC}). The correlation between solvent additive DPE and FF is related to the morphology of P*n*TIF:PCBM BHJ, and the solubility and the miscibility of individual P*n*TIF with either $PC_{61}BM$ or $PC_{71}BM$ play an important role in the thin film morphology and hence the FF of P*n*TIF:PCBM PSCs. To probe the thin film morphology and to understand its correlation with the FF, the corresponding results from the measurements of atomic force microscopy (AFM) and transmission electron microscopy (TEM) as well as grazing incidence wide-angle X-ray scattering (GIWAXS) are shown in Sections 3.5 and 3.6, respectively. Nevertheless, it is worth noting that the highest PCE of 10.69% among all the devices reported here was achieved with **P4TIF**:$PC_{61}BM$ PSCs without any solvent additive. The *J*–*V*

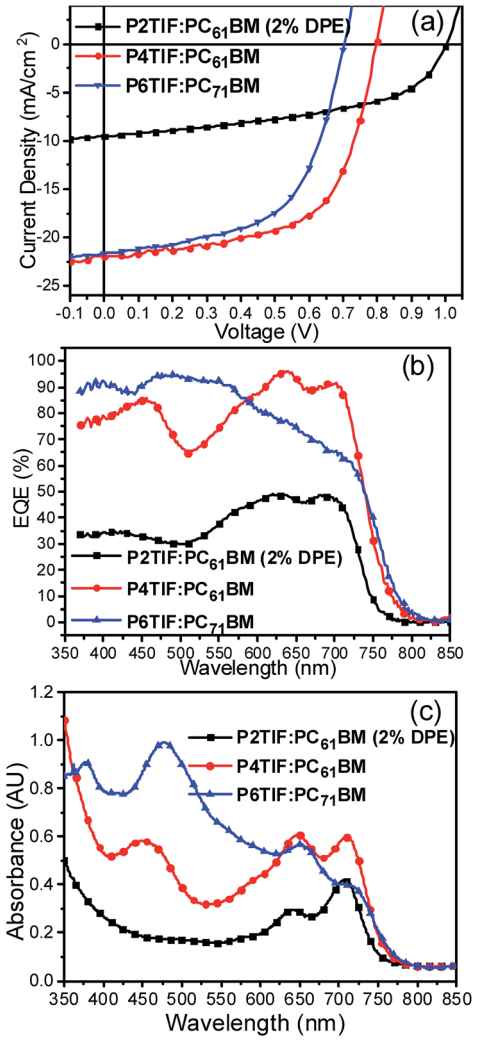

Fig. 2 (a) *J*–*V* curve of the best PSCs. (b) IPCE of the device with optimized active layers. (c) Thin film absorption spectra of P*n*TIF:PCBM with the same thickness ratio, *i.e.*, 160 : 300 : 365, as those of optimized active layers.

Table 2 Photovoltaic properties of PSCs based on P*n*TIF/PCBM with different combinations

Active layers[a]	Thickness [nm]	V_{OC}[b] [V]	J_{SC}[b] [mA cm^{-2}]	FF[b] [%]	PCE[b] [%]
P2TIF:$PC_{61}BM$	165	1.02 ± 0.01 (1.02)	6.95 ± 0.42 (7.47)	46.28 ± 2.47 (48.14)	3.27 ± 0.28 (3.67)
P2TIF:$PC_{71}BM$	165	1.00 ± 0.01 (1.00)	6.23 ± 0.69 (6.83)	44.38 ± 1.61 (43.18)	2.76 ± 0.23 (2.95)
P2TIF:$PC_{61}BM$ (2% DPE)	160	1.01 ± 0.01 (1.01)	9.47 ± 0.48 (9.50)	47.47 ± 1.82 (49.28)	4.52 ± 0.15 (4.73)
P4TIF:$PC_{61}BM$	300	0.81 ± 0.00 (0.80)	20.97 ± 0.66 (21.97)	59.90 ± 1.74 (60.82)	10.16 ± 0.28 (10.69)
P4TIF:$PC_{71}BM$	305	0.79 ± 0.00 (0.78)	19.93 ± 0.68 (20.98)	54.05 ± 1.34 (53.04)	8.47 ± 0.11 (8.68)
P4TIF:$PC_{61}BM$ (2% DPE)	300	0.80 ± 0.00 (0.80)	21.47 ± 0.54 (21.66)	54.81 ± 1.46 (56.87)	9.42 ± 0.24 (9.86)
P6TIF:$PC_{61}BM$	375	0.72 ± 0.00 (0.72)	18.10 ± 0.77 (18.42)	56.89 ± 1.61 (57.30)	7.41 ± 0.17 (7.60)
P6TIF:$PC_{71}BM$	365	0.70 ± 0.01 (0.71)	20.59 ± 0.61 (21.63)	57.29 ± 1.78 (57.35)	8.35 ± 0.25 (8.81)
P6TIF:$PC_{71}BM$ (2% DPE)	370	0.70 ± 0.01 (0.69)	21.27 ± 0.93 (22.10)	48.83 ± 1.68 (48.65)	7.22 ± 0.15 (7.42)

[a] All the active layers were fabricated with the same P*n*TIF:PCBM blending ratio of 1 : 1.5 (w/w). Depending on which P*n*TIF, the copolymer in P*n*TIF:PCBM spin-coating solution was optimized to the same concentration and the same optimized spin-coating condition (*i.e.*, spin rate). [b] The average value is obtained from over eight devices. The best device PCE value is shown in parentheses, and the corresponding V_{OC}, J_{SC}, and FF are shown in the parentheses as well.

characteristics of the best PSCs based on each P*n*TIF copolymers are shown in Fig. 2a.

Regarding the V_{OC} of P*n*TIF:PCBM PSCs, **P2TIF**:PCBM has a V_{OC} of around 1.00–1.02 V, which is larger than 0.79–0.81 V of **P4TIF**:PCBM, and which, in turn, is larger than 0.70–0.72 V of **P6TIF**:PCBM. Such a V_{OC} order is in accordance with the order of HOMO energy levels of P*n*TIF (see CV results in Section 3.3). Moreover, $PC_{71}BM$-based PSCs always have a smaller V_{OC} (by 0.01–0.02 V) than that of $PC_{61}BM$-based PSCs. It can be reasonably ascribed to a slightly lower LUMO energy level of $PC_{71}BM$ than $PC_{61}BM$.[41]

It is commonly known that a high J_{SC} of PSC requires an efficient photo-generated exciton, an efficient exciton dissociation, a less recombination of charge carriers, and a high charge transportation (mobility). The exciton dissociation and charge recombination of polymer:fullerene BHJ are closely related to the nano-fibril network and the degree of phase separation between polymer and fullerene materials,[42–44] which will be described and discussed later (see Section 3.5 TEM and AFM for details). Relevantly, the DPE solvent additive effectively worked for **P2TIF**:$PC_{61}BM$ PSCs in terms of enhancing the J_{SC} and FF of the PSCs. However, it did not work for **P4TIF**:$PC_{61}BM$ or **P6TIF**:$PC_{71}BM$ PSCs mainly due to the significant decrease in FF, which is related to the phase separation between P*n*TIF and PCBM and the optimal width of the nano-fibril. The corresponding discussion can also be found in Section 3.5 (AFM and TEM results).

Considering the absorption coefficient of P*n*TIF copolymer thin films (Fig. 1b), the long-wavelength light harvesting of **P2TIF** is better than that of **P4TIF** and **P6TIF**. However, the absorption spectra of P*n*TIF:PCBM blended thin films exhibited a weaker spectral intensity of **P2TIF**:$PC_{61}BM$ than those of **P4TIF**:$PC_{61}BM$ or **P6TIF**:$PC_{71}BM$ (Fig. 2c). This can be mainly attributed to the thinner **P2TIF**:$PC_{61}BM$ thin film (~160 nm) compared with that (>300 nm) of **P4TIF**:$PC_{61}BM$ or **P6TIF**:$PC_{71}BM$. In addition to a reason of thickness of the thin film, the observed much higher external quantum efficiency (EQE) spectra (Fig. 2b) over the whole range of 400–800 nm of **P4TIF**:$PC_{61}BM$ and **P6TIF**:$PC_{71}BM$ than **P2TIF**:$PC_{61}BM$ may be ascribed to the extended nano-fibrillar network and the high face-on alignment ratio of **P4TIF** and **P6TIF** (see Results and discussion of Sections 3.5, 3.6, and 3.7). Particularly, a very high EQE greater than 90% (Fig. 2b) or exceptional high thin film absorption intensity (Fig. 2c) around 450–580 nm was found for **P6TIF**:$PC_{71}BM$. In addition to a reason of thick active layer (~365 nm), these can be explained by a relatively higher absorption coefficient of **P6TIF** around 475 nm (Fig. 1b) as well as the absorption contribution of $PC_{71}BM$ in a range of 450–580 nm.[45] As many cases of PSCs having $PC_{71}BM$, $PC_{71}BM$ actually provides a photocurrent output of the solar cell due to its light absorption band of 450–580 nm. In the present study, the solubility of P*n*TIF in the processing solvent system is crucial to the thickness of P*n*TIF:PCBM BHJ. From other experimental evidences shown in this study, we have demonstrated the solubility of P*n*TIF to be **P6TIF** > **P4TIF** ≫ **P2TIF**, which is in accordance with the active layer thickness of the best device of each P*n*TIF. However, there is a clear trade-off between FF and J_{SC} in increasing the thickness of the BHJ, taking **P4TIF**:$PC_{61}BM$ as an example. As shown in Table 3, when the thickness of the **P4TIF**:$PC_{61}BM$ active layer increases from 120 nm to 300 nm, the FF reduced from 64.81 to 60.82%, whereas J_{SC} increases from 13.48 to 21.97 mA cm^{-2}. However, when the thickness is over 300 nm, both J_{SC} and FF decrease. **P4TIF** works better with such a thick active layer, which can be attributed to its favourable morphology (fine nano-fibrillar network) and high face-on crystalline orientation characteristics (see the discussion in Sections 3.5 and 3.6). Both factors sustain the elevation of J_{SC} in the thickness range of 120–300 nm. The optimal thickness of P*n*TIF:PCBM PSCs requires a fine-tuning, which has been achieved *via* the regulation of P*n*TIF:PCBM solution concentration. However, the solution concentration is very much limited to the solubility of P*n*TIF, of which **P2TIF** shows the lowest solubility and the thickness of the **P2TIF**:$PC_{61}BM$ active layer can hardly reach over 160 nm.

Table 3 Effect of the thickness of the active layer on the photovoltaic performance of the PSCs based on **P4TIF**:$PC_{61}BM$

Thickness[a] [nm]	V_{OC}[b] [V]	J_{SC}[b] [mA cm^{-2}]	Fill factor[b] [%]	PCE[b] [%]
380	0.80	20.83	47.78	7.96
355	0.80	21.61	50.76	8.78
300	0.80	21.97	60.82	10.69
260	0.81	20.55	61.16	10.18
190	0.81	17.65	62.50	8.93
120	0.82	13.48	64.81	7.16

[a] Various thicknesses of **P4TIF**:$PC_{61}BM$ active layers. [b] Data were collected from the device with best PCE.

As the results show, the highest J_{SC} of either **P4TIF**:$PC_{61}BM$ or **P6TIF**:$PC_{71}BM$ PSCs is over 21 mA cm^{-2}, which is a very high value among literature-reported polymer:$PC_{61}BM$ or $PC_{71}BM$-based BHJ PSCs. In summary, an extended nano-fibrillar network, a high face-on alignment ratio of the copolymer, and a thick active layer (>300 nm) of the BHJ are three good reasons for such high J_{SC}.

3.5 TEM and AFM morphology characterizations of P*n*TIF:PCBM

The morphologies of the P*n*TIF:PCBM blend films can be probed by TEM (Fig. 3). The bright and dark regions in bright-field TEM images represent copolymer and fullerene domains, respectively. Ideally, interpenetrating network structure with bicontinuous fine phase separation is the most favorable morphology for large area contacts of electron donor and electron acceptor materials as well as effective charge transport channels (or less charge recombination).

As shown in Fig. 3 (those without 2% DPE), all P*n*TIF copolymers form an interpenetrating network morphology with fibril-like nanostructures. However, the network structure of **P2TIF** is not quite the same as those of **P4TIF** and **P6TIF**. Compared with the fibril width of **P2TIF**, relatively finer nanofibrils of **P4TIF** and **P6TIF** can be clearly seen in Fig. 3. We attribute such difference mainly due to the solubility of P*n*TIF copolymers and hence their miscibility with PCBM.[43] In

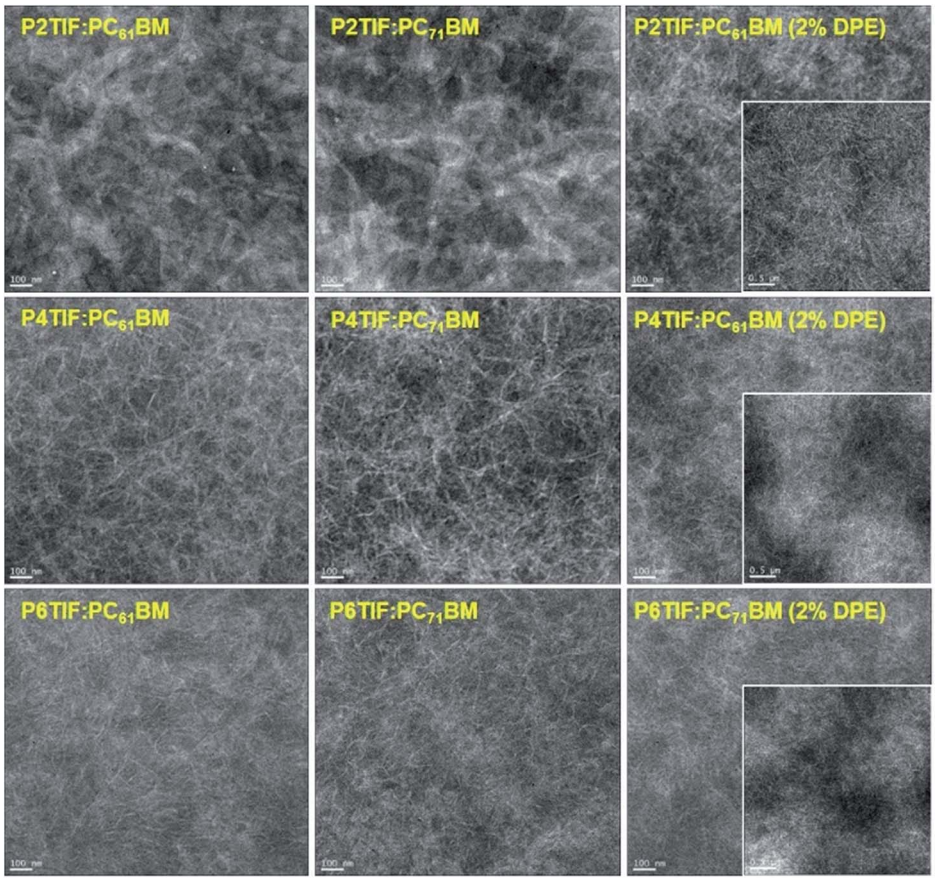

Fig. 3 TEM images of different P*n*TIF:PCBM thin films with or without 2% DPE. All scale bars are equivalent to a length of 100 nm (×40 000). The scale bars of three inserted figures are 0.5 μm in length (×10 000).

addition to a much thinner active layer in PSC, the poor solubility of **P2TIF** causes the formation of aggregate (nano-fibril) readily in the blended thin film, resulting in thick nano-fibrils in a less intertangling network structure. Estimated from our TEM images, **P4TIF** and **P6TIF** have a nano-fibril width of ≤10 nm. This width fits quite well to a typical exciton diffusion

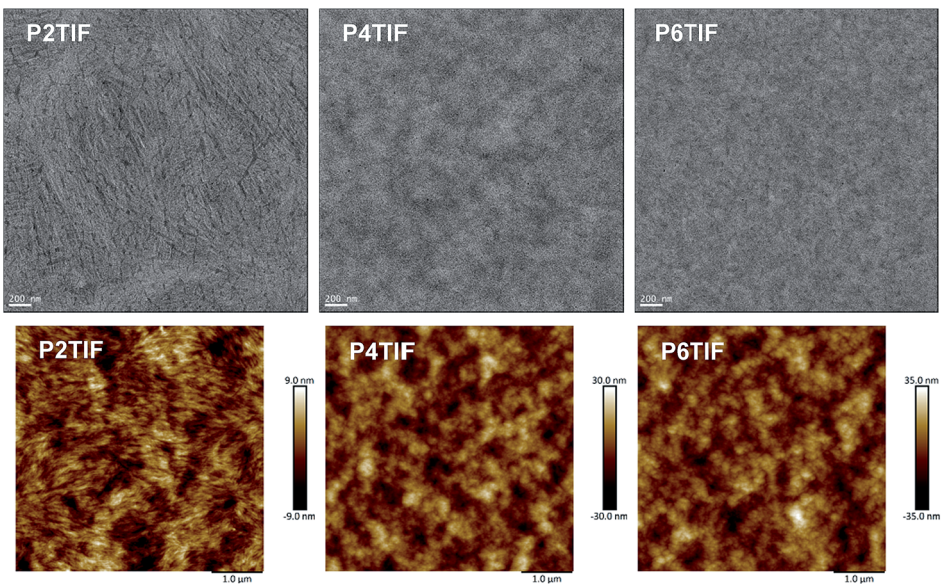

Fig. 4 (Top row) TEM images of P*n*TIF copolymer neat films. The scale bars are 200 nm (×20 000). (Bottom row) AFM images of P*n*TIF copolymer neat films. The scale bars are 1.0 μm.

length of π-conjugated polymers,[46] enabling efficient exciton dissociation and reducing exciton radiative recombination.[42] Besides, the finer nano-fibrils increase the area of the contact interface of P*n*TIF and PCBM, which facilitates the photocurrent generation. The poor solubility of **P2TIF** is also manifested in the TEM images of a copolymer neat film. The **P2TIF** neat film exhibits a thick and extended nano-fibrillar structure, which is not observed for **P4TIF** or **P6TIF** (Fig. 4). Similarly, the nano-fibrillar structure was found thicker and more extended for **P2TIF** than **P4TIF** or **P6TIF** neat films in AFM images (Fig. 4). One intriguing result of P*n*TIF:PCBM PSCs is the influence on PCE by using solvent additive DPE. The changes in TEM images due to the inclusion of DPE in P*n*TIF:PCBM blended thin films is quite relevant to the changes in PCE. As shown in Section 3.4, in enhancing PCE, the solvent additive DPE only works for **P2TIF**:$PC_{61}BM$ and does not work for either **P4TIF**:$PC_{61}BM$ or **P6TIF**:$PC_{71}BM$. Two crucial changes are revealed by the TEM images of the P*n*TIF:PCBM blended thin films with the inclusion of DPE. First, the width or the thickness of nano-fibril was reduced more significantly for **P2TIF**:PCBM than that for **P4TIF**:PCBM or **P6TIF**:PCBM. Second, phase separation between P*n*TIF-enriched and PCBM-enriched substances (bright and dark area in TEM images) was found to be more for **P4TIF**:$PC_{61}BM$ or **P6TIF**:$PC_{71}BM$ than **P2TIF**:$PC_{61}BM$. We suggest that solvent additive DPE interferes the strong aggregate tendency (to form nano-fibril) of **P2TIF**, whereas the interference is less significant due to the less tendency of aggregate (because of better solubility) of **P4TIF** or **P6TIF**. Moreover, in the presence of DPE, a bundle of nano-fibril is more mobile for **P4TIF** or **P6TIF** than that for **P2TIF** because of less structural rigidity of the former two copolymers. Therefore, with 2% DPE, the TEM images exhibit more phase separation (assembly of nano-fibril bundles) for **P4TIF**:$PC_{61}BM$ or **P6TIF**:$PC_{71}BM$ than **P2TIF**:$PC_{61}BM$ (the inserted figures in Fig. 3 or their full-scale pictures in Fig. S11†). In fact, the observation of surface morphology from AFM (Fig. S12†) is consistent with TEM results. With the solvent additive DPE in the process of thin film preparation, a root-mean-square (RMS) roughness of the AFM image decreases for **P2TIF**:$PC_{61}BM$ but increases for both **P4TIF**:$PC_{61}BM$ and **P6TIF**:$PC_{71}BM$, evident for the increase in phase separation.

Another unusual result from P*n*TIF:PCBM PSCs is that $PC_{71}BM$ outperforms $PC_{61}BM$ but for **P6TIF** only. We can attribute such unusual result to the miscibility difference between P*n*TIF and PCBM, which is very much related to the structural flexibility and hence the solubility of P*n*TIF (in either DCB or DPE).[34,35] From TEM images (Fig. 3), the width of nano-fibril is apparently lager for **P2TIF**:$PC_{71}BM$ and **P4TIF**:$PC_{71}BM$ than that for **P2TIF**:$PC_{61}BM$ and **P4TIF**:$PC_{61}BM$. In contrast, the width of nano-fibril of **P6TIF**:$PC_{71}BM$ is not much different from that of **P6TIF**:$PC_{61}BM$. As we have demonstrated already that the solubility of **P6TIF** is the best among P*n*TIF, the good solubility makes a similar miscibility of **P6TIF** to $PC_{71}BM$ or $PC_{61}BM$. Since such variation in nano-fibrillar width is in parallel with the variation of FF (Table 2), we infer that the best soluble P*n*TIF, **P6TIF**, has a best miscibility with $PC_{71}BM$ and only **P6TIF** PSC can have an increased FF when switching PCBM from $PC_{61}BM$ to $PC_{71}BM$.

3.6 GIWAXS characterization of crystallinity and chain-orientation of P*n*TIF

The corresponding data of GIWAXS measurement are summarized in Table 4. Fig. 5a–c exhibit the 2D-GIWAXS patterns of **P2TIF**:$PC_{61}BM$, **P4TIF**:$PC_{61}BM$, and **P6TIF**:$PC_{71}BM$ blend films. All the blend films show (100), (200), and (010) diffraction signals.

Table 4 2D-GIWAXS data of P*n*TIF neat film and PCBM blend film, with and without 2% DPE for PSCs; 2D-GIWAXS data of P*n*TIF neat films after thermal annealing for TFTs

P*n*TIF & P*n*TIF PSCs	$q_{(100)}$[a] [Å^{-1}]	$d_{(100)}$[b] [Å]	$q_{(010)}$[a] [Å^{-1}]	$d_{(010)}$[b] [Å]	A_{xy}/A_z (face-on/edge-on)[c]	Face-on$_{(100)}$ percentage[c] [%]	CCL$_{(100)}$[d] [Å]
P2TIF	0.282	22.3	1.748	3.60	0.20	16.8	127.4
P2TIF (2% DPE)	0.278	22.6	1.748	3.60	0.48	32.4	68.2
P4TIF	0.244	25.7	1.721	3.65	0.70	41.1	67.5
P6TIF	0.240	26.1	1.695	3.71	2.05	67.3	54.2
P2TIF:$PC_{61}BM$	0.282	22.3	1.770	3.55	0.39	28.0	85.4
P2TIF:$PC_{61}BM$ (2% DPE)	0.278	22.6	1.770	3.55	0.53	34.7	71.5
P4TIF:$PC_{61}BM$	0.244	25.7	1.736	3.62	0.77	43.5	67.3
P4TIF:$PC_{61}BM$ (2% DPE)	0.232	27.1	1.736	3.62	0.70	41.2	65.7
P6TIF:$PC_{71}BM$	0.237	26.6	1.763	3.56	0.91	47.8	54.1
P6TIF:$PC_{71}BM$ (2% DPE)	0.228	27.6	1.763	3.56	0.78	43.8	50.1

P*n*TIF TFTs (therm. annealed temperature)	$q_{(100)}$[a] [Å^{-1}]	$q_{(200)}$[a] [Å^{-1}]	$q_{(300)}$[a] [Å^{-1}]	$q_{(400)}$[a] [Å^{-1}]	$d_{(100)}$[b] [Å]	CCL$_{(100)}$[d] [Å^{-1}]
P2TIF (TA 240 °C)[e]	0.254	0.527	0.781	—	24.8	204.1
P4TIF (TA 240 °C)[e]	0.217	0.449	0.681	0.906	29.0	303.7
P6TIF (TA 210 °C)[e]	0.221	0.466	0.689	—	28.4	126.9

[a] Maximum of the diffraction peaks. [b] Calculated from q. [c] Estimated from the azimuthal angle scan of (100) diffraction peak. [d] Crystallite correlation length (CCL) estimated from (100) diffraction peak. [e] Thermally annealed (TA) P*n*TIF copolymer neat films under vacuum at high temperatures as marked for 1 hour.

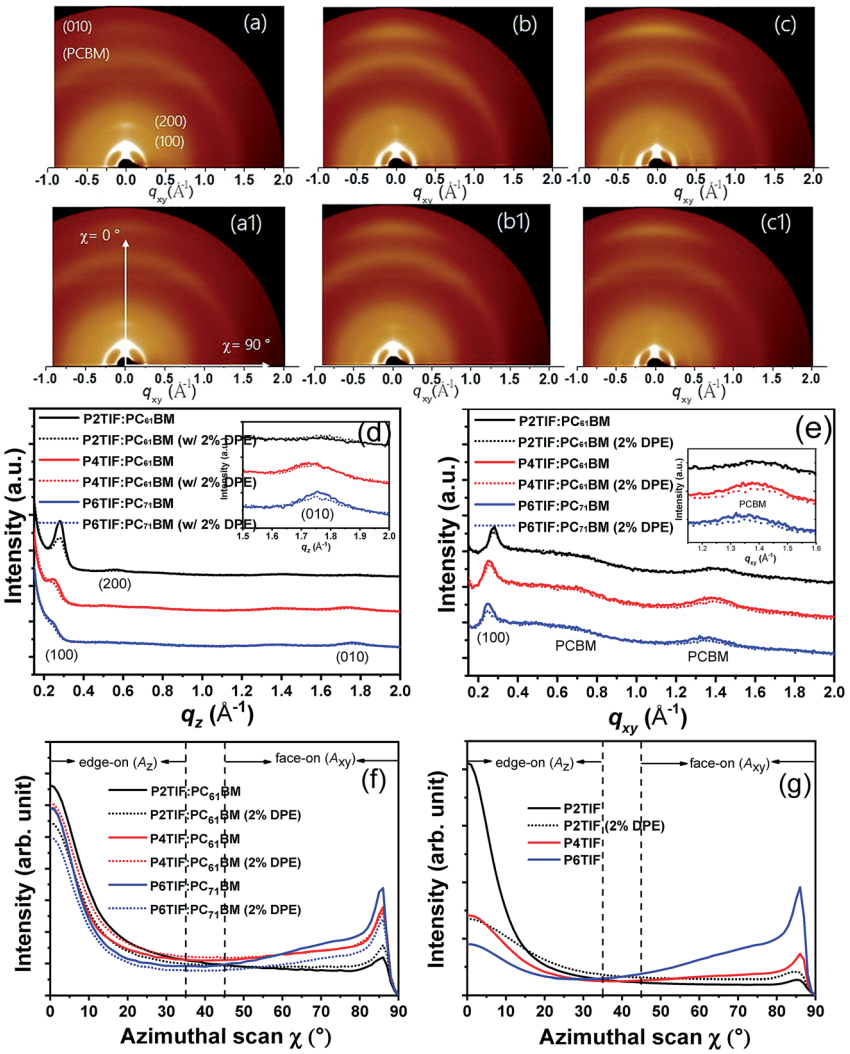

Fig. 5 2D-GIWAXS patterns of **P2TIF**:$PC_{61}BM$ without (a) and with (a1) 2% DPE, **P4TIF**:$PC_{61}BM$ without (b) and with (b1) 2% DPE, and **P6TIF**:$PC_{71}BM$ without (c) and with (c1) 2% DPE. The GIWAXS profiles of (d) out-of-plane direction (area integration $\chi = 0–45°$), (e) in-plane direction (area integration $\chi = 45–90°$), (f) azimuthal angle scans extracted from the lamellar (100) diffraction of P*n*TIF:PCBM blend films, (g) azimuthal angle scans extracted from the lamellar (100) diffraction of P*n*TIF neat films.

Fig. 5d and e exhibit the GIWAXS profiles of out-of-plane direction (integrated from the azimuthal scan range $\chi = 0–45°$) and in-plane direction (integrated from the azimuthal scan range $\chi = 45–90°$) from the 2D diffraction patterns, respectively. The (h00) diffraction signals are usually ascribed to the lamellar polymer side chain packing, and the (0k0) diffraction signal is corresponding to the π–π (face-to-face) stacking of the polymer backbone,[47] corresponding to a *d*-spacing of 22.3–27.6 Å ($d_{(100)}$) and 3.55–3.62 Å ($d_{(010)}$), respectively.

Clearly shown in Fig. 5d, **P2TIF**:$PC_{61}BM$ exhibits a significantly higher intensity of (100) diffraction and a significantly shorter lamellar *d*-spacing than those of **P4TIF**:$PC_{61}BM$ and **P6TIF**:PC_{71}-BM, indicating a larger crystalline domain and a dense crystallite lamellar packing. The good crystallinic nature of **P2TIF** in lamellar packing is also evident from its (200) diffraction, which is more distinguishable than that of **P4TIF** or **P6TIF**. Moreover, **P6TIF**:$PC_{71}BM$ exhibits a stronger (010) diffraction than the other two, indicating a larger crystallinic domain of **P6TIF** in the π–π stacking. Accordingly, the crystallinity nature of **P4TIF** is in between that of **P2TIF** and **P6TIF**. In fact, the size of the P*n*TIF:PCBM crystallite can be more quantitatively analyzed through the crystallite correlation length (CCL) by the Scherrer equation.[48] The prominent (100) diffraction peaks enable a reliable estimation of $CCL_{(100)}$ values and they are 85.4 Å, 67.3 Å, and 54.1 Å for **P2TIF**:$PC_{61}BM$, **P4TIF**:$PC_{61}BM$, and **P6TIF**:$PC_{71}BM$, respectively. The size of a crystallite (lamellar packing structure) from large to small is in an order of **P2TIF** > **P4TIF** > **P6TIF**. In fact, such an order is exactly reverse to the order of P*n*TIF solubility, which in turn is parallel with the number of flexible and non-planar 3-dodecylthiophene spacers in the copolymer main-chain. When DPE solvent additive is included in the thin film preparation, all $CCL_{(100)}$ and hence the size of crystalline domain get smaller, 71.5 Å, 65.7 Å, and 50.1 Å for **P2TIF**:$PC_{61}BM$, **P4TIF**:$PC_{61}BM$, and **P6TIF**:$PC_{71}BM$, respectively (Table 4).

The difference in the chain-orientation of each P*n*TIF mixed with PCBM can be clearly seen in the azimuthal angle (χ) scans of the lamellar (100) diffraction (Fig. 5f). The face-on ratio$_{(100)}$ can be estimated by calculating the area ratio of the χ between 45° and 90° to that between 0° and 45°.[49] Otherwise, the area integral ratio of χ ranges between 45° and 90° (A_{xy}) and 0° and 35° (A_z), *i.e.*, A_{xy}/A_z, corresponds to the fractions of face-on and edge-on crystallites.[12,13] The face-on ratio$_{(100)}$ or A_{xy}/A_z observed are 43.5%, 47.8%, and 28.0% or 0.77, 0.91 and 0.39 for **P4TIF**:$PC_{61}BM$, **P6TIF**:$PC_{71}BM$, and **P2TIF**:$PC_{61}BM$ without solvent additive DPE, respectively (Table 4). First, except for **P2TIF**:$PC_{61}BM$, these values are all higher than those (polymers for the thin film transistor or polymers for PSCs with thick BHJ) reported in the literature.[12,13,49] Second, our GIWAXS-measured face-on ratio$_{(100)}$ or A_{xy}/A_z of P*n*TIF neat films (*i.e.*, thin films without PCBM) is particularly high, 67.3% or 2.05, for **P6TIF** but it is particularly low, 16.8% or 0.20, for **P2TIF** (see Table 4, Fig. 5g and S13†). Such results indicate that P*n*TIF have a different preference of copolymer chain-orientation, particularly, a face-on and an edge-on alignment for **P6TIF** and **P2TIF**, respectively. From a chemical structure perspective, such GIWAXS results also imply that more the 3-dodecylthiophene spacers put in the copolymer main-chain, the more the face-on orientation can be expected for P*n*TIF. Finally, it is interesting to find that the face-on ratio$_{(100)}$ or A_{xy}/A_z gets increased for **P2TIF**:$PC_{61}BM$ when solvent additive DPE is included in the process of thin film preparation (see Table 4 and Fig. 5f). In contrast, the face-on ratio$_{(100)}$ or A_{xy}/A_z is actually decreased for **P4TIF**:$PC_{61}BM$ and **P6TIF**:$PC_{71}BM$. Importantly, such a difference in chain orientation is in parallel to the changes in PCE, *i.e.*, increased PCE for **P2TIF**:$PC_{61}BM$ but decreased PCE for both **P4TIF**:$PC_{61}BM$ and **P6TIF**:$PC_{71}BM$ when DPE is included in device fabrication. In addition to the increase in light-harvesting, face-on oriented copolymers will be more favourable in charge transport and the output photocurrent of PSCs.

3.7 SCLC and TFT characterization of hole mobility

The space-charge-limited current (SCLC)-determined hole mobilities ($\mu_{h,SCLC}$) of P*n*TIF neat films from high to low follows the order **P6TIF** (4.15×10^{-4} cm^2 V^{-1} s^{-1}) > **P4TIF** (3.14×10^{-4} cm^2 V^{-1} s^{-1}) > **P2TIF** (1.18×10^{-4} cm^2 V^{-1} s^{-1}) (Fig. S14 and Table S1†). Such order of $\mu_{h,SCLC}$ is in fact reverse to that of CCL$_{(100)}$ (crystallinity of the lamella stacking of copolymer), but it is parallel to the order of face-on ratio$_{(100)}$ or A_{xy}/A_z of P*n*TIF neat films estimated by GIWAXS (Table 4). Therefore, we may logically suggest that the face-on orientation of the copolymer chain plays a more important role than the size of the crystallite of lamellar stacking structure in the SCLC measurement. The face-on ratio$_{(100)}$ of P*n*TIF, **P6TIF** ≫ **P4TIF** > **P2TIF** (Fig. 5g and S13†), still influences the hole mobility determined by the thin film transistor (TFT) method, where the hole mobility is measured in a direction parallel to the substrate surface, the octadecylsilane-modified Si-wafer, different from that of SCLC measurement. From the GIWAXS measurement of P*n*TIF neat films on octadecylsilane-modified Si-wafer (Fig. 6), except for **P6TIF**, P*n*TIF all have a predominant edge-on orientation. There are still some minor face-on orientations or in-plane (100) diffraction signals for **P6TIF** (Fig. 6c and e), consistent with its strong preference of face-on orientation.

In addition, with thermal annealing treatment on P*n*TIF thin films, the CCL$_{(100)}$ of the P*n*TIF neat films all increased significantly from 127 to 204 Å, from 67.5 to 304 Å, and from 54 to 127 Å for **P2TIF**, **P4TIF**, and **P6TIF**, respectively (Table 4). Such CCL$_{(100)}$ results are very much in accordance with the thermal heating susceptibility in terms of the lamellar packing

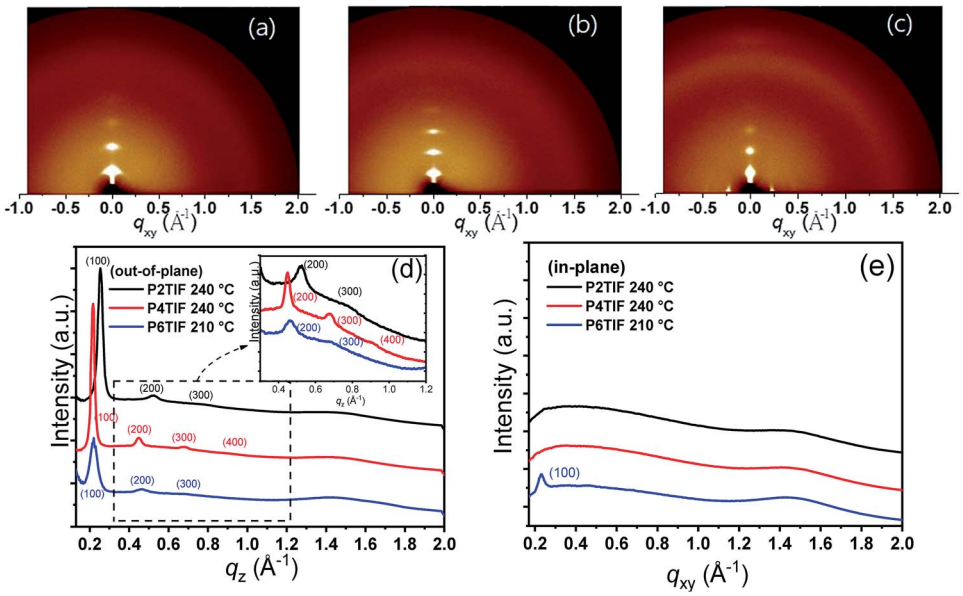

Fig. 6 2D-GIWAXS patterns of P*n*TIF copolymer neat films after thermal annealing: (a) **P2TIF**; (b) **P4TIF**; (c) **P6TIF**; the GIWAXS profiles of (d) out-of-plane direction (area integration χ = 0–45°) and (e) in-plane direction (area integration χ = 45–90°).

structure of P*n*TIF. With thermal heating, **P2TIF** has a moderate migration (and hence limited increase in $CCL_{(100)}$) due to its rigid structure of the copolymer backbone; **P6TIF** is too flexible and its conformation (of 3-dodecylthiophene spacer) disorder limits the increase in $CCL_{(100)}$. Moreover, **P6TIF** has the highest face-on orientation, which is adverse to the TFT hole mobility. Therefore, with thermal heating, **P4TIF** has the largest increase in $CCL_{(100)}$, and a TFT hole mobility ($\mu_{h,TFT}$) of 0.40 $cm^2 V^{-1} s^{-1}$, higher than 0.25 and 0.18 $cm^2 V^{-1} s^{-1}$ of **P2TIF** and **P6TIF**, respectively (Fig. S15 and Table S1†). Both hole mobility measurements of SCLC and TFT indirectly verified the preference of the face-on orientation of **P4TIF** and **P6TIF** in the PCBM blended film, which was observed in the GIWAXS measurement.

4. Conclusions

In summary, HOMO energy level engineering and the fine-tuning of solubility as well as crystallinity and the copolymer-chain orientation of P*n*TIF copolymers was realized by introducing flexible, non-planar, electron-rich 3-dodecylthiophene spacers along with the copolymer main-chains. Although it increases the HOMO energy level and hence decreases the V_{OC} value of PSCs, the 3-dodecylthiophene spacers could enhance the solubility and miscibility (with PCBM) in the thin film of P*n*TIF:PCBM. First, PSCs with a thick active layer (≥300 nm) were fabricated with **P4TIF** or **P6TIF** mainly due to the satisfactory solubility. Second, carefully examined by TEM and AFM, **P4TIF** or **P6TIF** formed favorable thin film morphologies with $PC_{61}BM$ or $PC_{71}BM$ in a fine nano-fibrillar network structure, resulting in a much higher J_{SC} and FF of **P4TIF** and **P6TIF** PSCs compared with those of **P2TIF**. Moreover, GIWAXS measurement verified the high face-on chain orientation (>40%) found for the thin film of **P4TIF**:$PC_{61}BM$ and **P6TIF**:$PC_{71}BM$, facilitating the light harvesting of the PSCs. **P4TIF**:$PC_{61}BM$ and **P6TIF**:$PC_{71}BM$ PSCs show high J_{SC} over 21 mA cm^{-2} and EQE as high as >90%. With optimal trade-off between V_{OC} and J_{SC} as well as FF, **P4TIF**:$PC_{61}BM$ PSCs achieved the highest PCE of 10.69%, which was one of the best devices among the thick (≥300 nm), single-junction, fullerene-based PSCs. Therefore, in the present study, we have successfully demonstrated that the isoindigo unit can be an effective option for the structural design of acceptor units in addition to TT, BDD, BT, and NTz.

Conflicts of interest

There are no conflicts to declare.

Acknowledgements

We gratefully thank Mr Shih-Hsin Huang (Institute of Chemistry, Academia Sinica) for helping the experiments in TEM. We thank Academia Sinica for financial support in part by the project of Taiwan's Deep Decarbonization Pathways toward a Sustainable Society and Sustainability Science Research Program of Academia Sinica.

Notes and references

1 J. Zhao, Y. Li, G. Yang, K. Jiang, H. Lin, H. Ade, W. Ma and H. Yan, *Nat. Energy*, 2016, **1**, 15027–15033.
2 H. Chen, Z. Hu, H. Wang, L. Liu, P. Chao, J. Qu, W. Chen, A. Liu and F. He, *Joule*, 2018, **2**, 1623–1634.
3 S. Li, L. Ye, W. Zhao, H. Yan, B. Yang, D. Liu, W. Li, H. Ade and J. Hou, *J. Am. Chem. Soc.*, 2018, **140**, 7159–7167.
4 S. Zhang, Y. Qin, J. Zhu and J. Hou, *Adv. Mater.*, 2018, **30**, 1800868.
5 Z. Zheng, Q. Hu, S. Zhang, D. Zhang, J. Wang, S. Xie, R. Wang, Y. Qin, W. Li, L. Hong, N. Liang, F. Liu, Y. Zhang, Z. Wei, Z. Tang, T. P. Russell, J. Hou and H. Zhou, *Adv. Mater.*, 2018, **30**, 1801801.
6 J. Yuan, Y. Zhang, L. Zhou, G. Zhang, H.-L. Yip, T.-K. Lau, X. Lu, C. Zhu, H. Peng, P. A. Johnson, M. Leclerc, Y. Cao, J. Ulanski, Y. Li and Y. Zou, *Joule*, 2019, **3**, 1140–1151.
7 B. Fan, D. Zhang, M. Li, W. Zhong, Z. Zeng, L. Ying, F. Huang and Y. Cao, *Sci. China: Chem.*, 2019, **62**, 746–752.
8 B. Fan, L. Ying, P. Zhu, F. Pan, F. Liu, J. Chen, F. Huang and Y. Cao, *Adv. Mater.*, 2017, **29**, 1703906.
9 H. Yao, F. Bai, H. Hu, L. Arunagiri, J. Zhang, Y. Chen, H. Yu, S. Chen, T. Liu, J. Y. L. Lai, Y. Zou, H. Ade and H. Yan, *ACS Energy Lett.*, 2019, **4**, 417–422.
10 Y. Liu, J. Zhao, Z. Li, C. Mu, W. Ma, H. Hu, K. Jiang, H. Lin, H. Ade and H. Yan, *Nat. Commun.*, 2014, **5**, 5293.
11 H. Hu, K. Jiang, G. Yang, J. Liu, Z. Li, H. Lin, Y. Liu, J. Zhao, J. Zhang, F. Huang, Y. Qu, W. Ma and H. Yan, *J. Am. Chem. Soc.*, 2015, **137**, 14149–14157.
12 V. Vohra, K. Kawashima, T. Kakara, T. Koganezawa, I. Osaka, K. Takimiya and H. Murata, *Nat. Photonics*, 2015, **9**, 403–408.
13 K. Kawashima, T. Fukuhara, Y. Suda, Y. Suzuki, T. Koganezawa, H. Yoshida, H. Ohkita, I. Osaka and K. Takimiya, *J. Am. Chem. Soc.*, 2016, **138**, 10265–10275.
14 Y. Jin, Z. Chen, S. Dong, N. Zheng, L. Ying, X.-F. Jiang, F. Liu, F. Huang and Y. Cao, *Adv. Mater.*, 2016, **28**, 9811–9818.
15 J. Lee, D. H. Sin, B. Moon, J. Shin, H. G. Kim, M. Kim and K. Cho, *Energy Environ. Sci.*, 2017, **10**, 247–257.
16 X. Ouyang, R. Peng, L. Ai, X. Zhang and Z. Ge, *Nat. Photonics*, 2015, **9**, 520–524.
17 Z. He, B. Xiao, F. Liu, H. Wu, Y. Yang, S. Xiao, C. Wang, T. P. Russell and Y. Cao, *Nat. Photonics*, 2015, **9**, 174–179.
18 J.-D. Chen, C. Cui, Y.-Q. Li, L. Zhou, Q.-D. Ou, C. Li, Y. Li and J.-X. Tang, *Adv. Mater.*, 2015, **27**, 1035–1041.
19 H. Zhong, L. Ye, J.-Y. Chen, S. B. Jo, C.-C. Chueh, J. H. Carpenter, H. Ade and A. K.-Y. Jen, *J. Mater. Chem. A*, 2017, **5**, 10517–10525.
20 H. Kim, B. Lim, H. Heo, G. Nam, H. Lee, J. Y. Lee, J. Lee and Y. Lee, *Chem. Mater.*, 2017, **29**, 4301–4310.
21 T. Liu, X. Pan, X. Meng, Y. Liu, D. Wei, W. Ma, L. Huo, X. Sun, T. H. Lee, M. Huang, H. Choi, J. Y. Kim, W. C. H. Choy and Y. Sun, *Adv. Mater.*, 2017, **29**, 1604251.
22 Z. Li, D. Yang, X. Zhao, T. Zhang, J. Zhang and X. Yang, *Adv. Funct. Mater.*, 2018, **28**, 1705257.

23 E. Wang, Z. Ma, Z. Zhang, K. Vandewal, P. Henriksson, O. Inganäs, F. Zhang and M. R. Andersson, *J. Am. Chem. Soc.*, 2011, **133**, 14244–14247.
24 Z. Ma, W. Sun, S. Himmelberger, K. Vandewal, Z. Tang, J. Bergqvist, A. Salleo, J. W. Andreasen, O. Inganäs, M. R. Andersson, C. Müller, F. Zhang and E. Wang, *Energy Environ. Sci.*, 2014, **7**, 361–369.
25 C.-C. Ho, C.-A. Chen, C.-Y. Chang, S. B. Darling and W.-F. Su, *J. Mater. Chem. A*, 2014, **2**, 8026–8032.
26 E. Wang, W. Mammo and M. R. Andersson, *Adv. Mater.*, 2014, **26**, 1801–1826.
27 W. Yue, R. S. Ashraf, C. B. Nielsen, E. Collado-Fregoso, M. R. Niazi, S. A. Yousaf, M. Kirkus, H.-Y. Chen, A. Amassian, J. R. Durrant and I. McCulloch, *Adv. Mater.*, 2015, **27**, 4702–4707.
28 G. E. Park, S. Choi, J. Shin, M. J. Cho and D. H. Choi, *Org. Electron.*, 2016, **34**, 157–163.
29 H. Hu, K. Jiang, J.-H. Kim, G. Yang, Z. Li, T. Ma, G. Lu, Y. Qu, H. Ade and H. Yan, *J. Mater. Chem. A*, 2016, **4**, 5039–5043.
30 H. Mori, S. Hara, S. Nishinaga and Y. Nishihara, *Macromolecules*, 2017, **50**, 4639–4648.
31 E. H. Jung, H. Ahn, W. H. Jo, J. W. Jo and J. W. Jung, *Dyes Pigm.*, 2019, **161**, 113–118.
32 C. Wang, B. Zhao, Z. Cao, P. Shen, Z. Tan, X. Li and S. Tan, *Chem. Commun.*, 2013, **49**, 3857–3859.
33 X. Sun, Z. Zhang, R. Hou, M. Huang, B. Zhao and S. Tan, *Dyes Pigm.*, 2017, **139**, 403–411.
34 E. H. Jung and W. H. Jo, *Energy Environ. Sci.*, 2014, **7**, 650–654.
35 Y. Deng, W. Li, L. Liu, H. Tian, Z. Xie, Y. Geng and F. Wang, *Energy Environ. Sci.*, 2015, **8**, 585–591.
36 S.-F. Liao, C.-T. Chen and C.-Y. Chao, *ACS Macro Lett.*, 2017, **6**, 969–974.
37 J. W. Jo, J. W. Jung, E. H. Jung, H. Ahn, T. J. Shin and W. H. Jo, *Energy Environ. Sci.*, 2015, **8**, 2427–2434.
38 M. L. Keshtov, S. A. Kuklin, N. A. Radychev, A. Y. Nikolaev, E. N. Koukaras, A. Sharma and G. D. Sharma, *RSC Adv.*, 2016, **6**, 14893–14908.
39 J. W. Jo, J. W. Jung, H.-W. Wang, P. Kim, T. P. Russell and W. H. Jo, *Chem. Mater.*, 2014, **26**, 4214–4220.
40 A. K. K. Kyaw, D. H. Wang, V. Gupta, J. Zhang, S. Chand, G. C. Bazan and A. J. Heeger, *Adv. Mater.*, 2013, **25**, 2397–2402.
41 A. S. Shalabi, S. Abdel Aal and M. M. Assem, *Nano Energy*, 2012, **1**, 608–623.
42 W. Li, K. H. Hendriks, A. Furlan, W. S. C. Roelofs, S. C. J. Meskers, M. M. Wienk and R. A. J. Janssen, *Adv. Mater.*, 2014, **26**, 1565–1570.
43 Y. Deng, Y. Chen, J. Liu, L. Liu, H. Tian, Z. Xie, Y. Geng and F. Wang, *ACS Appl. Mater. Interfaces*, 2013, **5**, 5741–5747.
44 W. Li, K. H. Hendriks, A. Furlan, W. S. C. Roelofs, M. M. Wienk and R. A. J. Janssen, *J. Am. Chem. Soc.*, 2013, **135**, 18942–18948.
45 M. M. Wienk, J. M. Kroon, W. J. H. Verhees, J. Knol, J. C. Hummelen, P. A. van Hal and R. A. J. Janssen, *Angew. Chem., Int. Ed.*, 2003, **42**, 3371–3375.
46 O. V. Mikhnenko, H. Azimi, M. Scharber, M. Morana, P. W. M. Blom and M. A. Loi, *Energy Environ. Sci.*, 2012, **5**, 6960–6965.
47 I. Osaka and K. Takimiya, *Polymer*, 2015, **59**, A1–A15.
48 H.-R. Tseng, H. Phan, C. Luo, M. Wang, L. A. Perez, S. N. Patel, L. Ying, E. J. Kramer, T.-Q. Nguyen, G. C. Bazan and A. J. Heeger, *Adv. Mater.*, 2014, **26**, 2993–2998.
49 Y. Kim, D. X. Long, J. Lee, G. Kim, T. J. Shin, K.-W. Nam, Y.-Y. Noh and C. Yang, *Macromolecules*, 2015, **48**, 5179–5187.

